Associations between iron oxyhydroxide nanoparticle growth and metal adsorption/structural incorporation

C. S. Kim[a], C. J. Lentini[a], and G.A. Waychunas[b]

[a] Department of Physical Sciences, Chapman University, Orange, CA 92866
[b] Earth Sciences Division, Lawrence Berkeley National Laboratory, Berkeley, CA 94720

Abstract

The interaction of metal ions and oxyanions with nanoscale mineral phases has not yet been extensively studied despite the increased recognition of their prevalence in natural systems as a significant component of geomedia. A combination of macroscopic uptake studies to investigate the adsorption behavior of As(V), Cu(II), Hg(II), and Zn(II) onto nanoparticulate goethite (α-FeOOH) as a function of aging time at elevated temperature (75°C) and synchrotron-based X-ray studies to track changes in both the sorption mode and the rate of nanoparticle growth reveal the effects that uptake has on particle growth. Metal(loid) species which sorb quickly to the iron oxyhydroxide particles (As(V), Cu(II)) appear to passivate the particle surface, impeding the growth of the nanoparticles with progressive aging; in contrast, species that sorb more slowly (Hg(II), Zn(II)) have considerably less impact on particle growth. Progressive changes in the speciation of these particular metals with time suggest shifts in the mode of metal uptake with time, possibly indicating structural incorporation of the metal(loid) into the nanoparticle; this is supported by the continued increase in uptake concomitant with particle growth, implying that metal species may transform from surface-sorbed species to more structurally incorporated forms. This type of incorporation would have implications for the long-term fate and mobility of metals in contaminated regions, and affect the strategy for potential remediation/modeling efforts.

1. Introduction

The processes of metal sorption to geomedia represent a critically important area in the field of environmental chemistry. In particular, the role of iron oxyhydroxides in these processes is significant due to their natural abundance in the environment and the strong affinity they possess for dissolved metal species, thus influencing the fate and transport of such pollutants. The initial rapid adsorption of metals onto iron oxyhydroxides can, with time and/or changing geochemical conditions, lead to slower rate-limiting uptake mechanisms including diffusion into micropores, (co-)precipitation, surface precipitation, and structural incorporation/substitution [1-6], further impacting the mobility, potential bioavailability, and long-term sequestration of metal contaminants.

A number of macroscopic uptake studies have been conducted demonstrating the behavior of metal uptake onto iron oxyhydroxide phases [7-13]. More recently, investigators have applied X-ray-based spectroscopic methods to study the precise mechanisms of metal uptake onto mineral surfaces at the atomic scale, gaining considerable insight into the different processes by which metals are transferred from the aqueous to the solid phase [14-20]. Few studies, however, have explored the interaction of metals with nanosized particles, which are postulated to be of particular importance and abundance in natural systems due to their extremely high surface areas, possible enhanced or altered reactivity (e.g. with metal sorbates), and long lifetimes in suspension, leading to long distance transfer in aqueous/subsurface systems [21-23]. Furthermore, nanoparticles are likely to aggregate and/or grow in natural settings, although the effects of these processes on either previously sorbed metals or the potential of such

multiparticle aggregates for additional uptake have not been characterized. Our initial studies suggest that with increasing particle size at the nanoscale, the mode of uptake may change subtly while the degree of surface coverage may actually increase, indicating that the mode and quantitative amount of uptake can vary with particle size [24]; other macroscopic studies also suggest differences in the pH-based uptake behavior of metals onto nanosized sorbents as a function of particle size and pH [25]. These recent findings further support the conjecture that nanoparticles may act and react in fundamentally distinct ways from those of their macroscale counterparts, hence motivating the current work.

The studies previously referenced establish the basis for combining traditional batch sorption experiments, used to characterize the general uptake behavior of metals onto nanoscale particles, with modern spectroscopic techniques designed to explore differences at the atomic level between the modes of metal sorption onto nanosized particles during growth. The primary goal of this work is to understand the behavior and speciation of metal uptake to nanoscale particles as they are growing, predicting that uptake will both increase and become more associated with structurally-incorporated species with continued growth; additionally, surface uptake is anticipated to have a measurable impact on the rate of nanoparticle growth, introducing surface poisoning/passivation effects that can inhibit both aggregation-based and ripening-based particle growth mechanisms. The determination of metal(loid)-specific behavior under these conditions is critical to predicting more accurately the mobility and availability of metals that sorb to nanoparticles and their larger-scale aggregates.

In this study, both macroscopic and spectroscopic strategies are applied to characterize the sorption and incorporation of four different metal(loid) ions (As(V), Cu(II), Hg(II), and Zn(II)) onto iron oxyhydroxide nanoparticles as a function of nanoparticle aging/growth induced by elevated temperature. Specifically, macroscopic uptake experiments are used to track changes in metal(loid) uptake as a function of time while synchrotron-based X-ray methods including micro-X-ray diffraction (μXRD) and extended X-ray absorption fine structure (EXAFS) spectroscopy are applied to explore both the structural/size evolution of particles as a function of contaminant uptake and the mode of metal uptake as a function of aging time. Together these methods can provide detailed macroscopic and atomic-level information on both the mechanisms of metal uptake onto nanoparticles and the related effects on the dynamic, growing substrate to which the metals are becoming incorporated.

Referring to the final chapter (entitled "Priorities for Future Metal Adsorption Research") of the original Adsorption of Metals by Geomedia volume [26], we have attempted to address some of the proposed goals and considerations for future adsorption research. System characterization was enhanced by addressing issues such as pH changes, Fe (III) release in response to cation adsorption, and aging time [27]. In an attempt to further comprehend metal adsorption to a single adsorbent (nanoscale goethite) a multi-metal data approach was taken as suggested by Kinniburgh *et al.*[28]. Lastly, time-dependent data were analyzed and transitions in modes of uptake were directly modeled using EXAFS spectroscopy.

2. Experimental Method

2.1 Nanoparticle Preparation

A suspension of goethite (α-FeOOH) nanoparticles was prepared according to Guyodo *et al.* [29] by first adding a 0.25 M $NaHCO_3$ solution dropwise to an equivalent volume of a 0.20 M $Fe(NO_3)_3$ solution in a LDPE screw-capped bottle, both solutions having been previously filtered through a 0.2 μm filter. The resulting mixture was then placed on an agitator for 30 minutes with periodic opening of the cap to release CO_2 buildup. Once gas release was minimized the solution was placed in a conventional kitchen microwave and heated at high power in intervals of 30 seconds, with periodic mixing between heating intervals, for a period of approximately 3 minutes or until boiling of the suspension had just begun. This procedure initiates nucleation of nanosized goethite particles [29]. The mixture was then immediately placed into an ice bath to halt the nanoparticle formation process; once cool, the solution was transferred to a 1000 MWCO dialysis tubing and submerged in a large volume of DI water which was replaced several times a day until reaching a pH of 5.0 ± 0.1. The resulting nanoparticle suspension was found through previous characterization [24] to be a monodisperse suspension of 5-nm diameter oblong particles with a solids concentration of 6.74 g/L and a BET surface area of 306 m^2/g. The initial unaged suspension was stored in a refrigerator at 4°C.

As a basis of comparison with the nanoparticulate goethite, a batch of macroscale goethite was prepared by base (NaOH) titration of a ferric nitrate solution followed by equilibration at 60°C and dialysis as described by Atkinson *et al.* [30], resulting in acicular needles of 200 x 30 nm dimensions and surface area of 91 m^2/g. So-called "2-line" ferrihydrite was also synthesized following the procedure of Schwertmann and

Cornell [31]. Eight grams of $Fe(NO_3)_3 \cdot 9\ H_2O$ was dissolved in 100 ml of deionized water and the pH adjusted to 7-8 using 1M KOH and vigorous stirring. Samples were placed into 50 ml centrifuge tubes, centrifuged for 15 minutes at 3000 RPM, and either washed with 45 mL of deionized water or dialyzed in a 1000 MWCO dialysis tubing to remove residual electrolytes before drying. No difference in the μXRD patterns of the ferrihydrite samples was observed as a function of the washing method.

2.2 Sample Preparation

Batch uptake experiments were performed in 1 L glass beakers with magnetic stir bars under ambient atmospheric conditions with a background electrolyte concentration of 0.1 M $NaNO_3$. Separate 400 ml portions of the initial nanoparticle suspension were first combined with 60 ml of 5mM solutions of $AsHNa_2O_4$ (374.6mg L^{-1}), $Cu(NO_3)_2$ (317.7mg L^{-1}), $Hg(NO_3)_2$ (1002mg L^{-1}) and $Zn(NO_3)_2$ (327.0mg L^{-1}). A fifth batch of nanogoethite was exposed to an equivalent volume of deionized water in place of the metal solutions and served as the control/blank for the experiment. Macroscopic uptake of each metal(loid) was induced by adding 0.1 M NaOH in 50uL aliquots to obtain a pH level of 6.0 ± 0.1; although the metal cations and oxyanions display opposite pH-dependent uptake behavior (with the cations exhibiting maximum sorption at high pH and the oxyanion at low pH), this pH level was determined through preliminary testing to achieve sufficient uptake for our experiments. Appropriate amounts of 0.5 M $NaNO_3$ and deionized water were added to adjust the ionic strength and metal(loid) concentration in the final metal and control solutions to 0.1 M and 0.5 mM, respectively, resulting in a final volume of 600 mL with a solids concentration of 4.49 g/L.

Following preparation, each metal suspension was separated into labeled 30 ml LDPE bottles with screw-cap lids. Samples were placed in a conventional laboratory oven or hot water bath/shaker at 78 ± 2°C to induce particle growth in the presence of the metal(loid), with samples collected at varying time intervals up to 7 days total duration. Our previous characterization of similar nanoparticle suspensions with μXRD, dynamic light scattering, transmission electron microscopy, and small- and wide-angle X-ray scattering suggest that nanoparticle aggregation plays a significant role in the early growth stages of the particles, although ripening-based growth may become a more significant process for the continued growth of the larger aggregates [24]. The resulting particle growth occurs at a considerably faster rate than at room temperature, where stable nanoclusters have been shown to persist in suspension for 10 weeks with minimal continued aggregation [32]. Upon removal from the elevated temperature conditions, suspensions were immediately centrifuged at 3000 RPM for 15 minutes and the supernatant decanted, recorded for pH level, filtered with a 0.2 μm filter, and acidified using 20 μL aliquots of concentrated HNO_3 until pH<2 prior to analysis by ICP-OES.

The centrifuged solids to be analyzed by μXRD were cleaned by resuspending the particles twice in 30 mL of deionized water followed by additional centrifugation and decanting. The washed pellets were then resuspended in a small volume of deionized water to maximize recovery from the centrifuge tubes and placed onto watch glasses to be dried in an oven overnight at 60°C. Once dry, samples were stored in individual capped glass vials for later μXRD analysis.

The centrifuged solids to be analyzed with EXAFS spectroscopy were spread on a filter paper to remove excess liquid, then loaded as moist pastes in Teflon sample holders

and sealed with Kapton tape. All "0 hr" samples were processed as quickly as possible with no subsequent heating; approximately 30 minutes elapsed between the preparation of the sample and the separation of pellet and supernatant.

2.3 Inductively Coupled Plasma Optical Emission Spectroscopy(ICP-OES) Analysis

A TJA IRIS Advantage/1000 Radial ICP Spectrometer was used to determine the metal(loid) concentrations in the filtered and acidified supernatants. Standards of 1, 10, and 100 ppm (mg/L) concentrations of the added metal(loid)s as well as Fe(III) were prepared under the same pH and ionic strength conditions as the samples for proper instrumental calibration prior to analysis. These residual metal(loid) concentrations measured in the supernatants were then used to calculate the percentage of metal(loid) uptake from solution assuming minimal uptake to vessel walls [18]. Supernatant Fe(III) concentrations were measured to assess the extent of nanoparticle dissolution or passage through the filters.

2.4 Synchrotron X-Ray Microdiffraction

Dried samples were powdered with a mortar and pestle, resuspended in 20 µL of ethanol and placed on a clean low-background quartz (111) C-cut single crystal to dry prior to µXRD analysis at bend magnet beamline 7.3.3 of the Advanced Light Source (ALS) at Lawrence Berkeley National Laboratory using a 4-crystal Si (111) monochromator tuned to an energy of 6000 eV. Diffraction images were collected for 1200 sec at a beam size of 7 x 10 µm onto a MAR CCD detector at a sample-detector distance of 136.617 mm. This analysis allowed data collection over a Q range of 1.3-3.7

$Å^{-1}$. A diffraction image was collected on a clean spot of the single crystal prior to sample data collection for background subtraction purposes.

Integration of the raw μXRD diffraction images was performed using X-ray Microdiffraction Analysis Software version 5.1 (X-MAS) [33] over a 2θ range of 25° – 75° and a chi range of -22 to -2 with a resolution of 0.100. The statistical software analysis program Origin 7.5 [34] was used to quantify the rate of nanoparticle growth through diffraction peak integration. The 001 diffraction peak was selected for integration and particle size analysis as it corresponds with the primary growth direction along the c-axis of goethite crystals [35]. Each integrated diffraction pattern was processed to minimize background variations and beam flux variability; the latter correction was accomplished by normalizing each data point by the beam intensity (I_o) recorded just prior to each data collection step.

Data were converted to Q-space and a Gaussian fit performed on the 001 peak. Following baseline subtraction of the fitted peak, Origin was used to calculate the integrated area of the peak as represented by the best possible Gaussian fit. As a proxy for tracking the growth rates of the nanoparticles along the c-axis, the ratio of the integrated area under the 001 peak (25° - 32° 2θ) to the integrated area of the entire dataset (25° - 75° 2θ), or A_{001} /A_{total}, was calculated and plotted for each set of aged samples. Application of the Scherrer equation to quantify particle size was found to be unreliable due to variability in baseline determinations and low absolute peak intensity, so this method was not applied.

2.5 X-Ray Absorption Spectroscopy

Based on results from the macroscopic uptake experiments which showed progressive uptake of Hg(II) and Zn(II) over time (see Results section), X-ray absorption spectroscopy (XAS) of selected Hg and Zn sorption samples was performed on wiggler-magnet beamlines 10-2 and 11-2 at Stanford Synchrotron Radiation Laboratory (SSRL). Samples were analyzed as moist pastes on either double Si 111 (BL 10-2) or Si 220 (BL 11-2) monochromator crystals detuned 30% down from the maximum beam intensity to reject higher-order harmonic signals. Zn K-edge (9659 eV) and Hg L_{III}-edge (12284 eV) XAS spectra were collected on samples at room temperature in fluorescence yield mode using a 13 (BL10-2) and 30 (BL 11-2) element high-throughput germanium detector. This technique is preferred over the use of transmission-collected data or ion-chamber collected fluorescence for low concentration samples [36, 37]. The samples were placed so that their normals were at a 45° angle to the incoming beam and the germanium detector window, in the plane of the synchrotron X-ray electric vector, so that elastic scattering from the sample was minimized. Aluminum filters and Soller slits were used to minimize Fe fluorescence and Soller slits to further limit elastic scattering from reaching the detector. [37]. Zn metal foil and $HgCl_2$ powder were used as monochromator energy calibration standards. The number of scans for each sample was determined by the amount of uptake measured through the macroscopic uptake experiments, with lower concentrations requiring additional scans; Zn samples required from 7-10 scans and Hg samples from 10-23 scans.

Data were analyzed using the SixPACK software package Version 0.57 [38]. Each XAS scan was calibrated in energy by using the first derivative of the relevant calibration standard to detect any changes in assigned monochromator energy, and then

correct data scans accordingly. To insure correct amplitude measurements of EXAFS spectra due to detector deadtime, sample spectra collected at BL 11-2 were deadtime-corrected from reference data in the SamView interface and then averaged into one file. Background subtraction was automatically performed (k-weighting = 3, R background = 1 Å) using the automatic background removal algorithm in SixPACK and the resulting spectra were fit using a spline with an average of 8 spline knots. After removal of the spline-fit background function the data were converted to k-space with a k^3 weighting. Prior to k-space fitting, the spectra were then Fourier-transformed to produce EXAFS structure functions. Fitting was performed over a k-range of 2-12 $Å^{-1}$ for Hg and 3-10.5 $Å^{-1}$ for Zn while the R-range was from 0-4 Å for all samples.

EXAFS single scattering paths used to fit the background subtracted, k^3-weighted data were created in SixPACK using FEFF 6l [39]. The approach to fitting EXAFS spectra was to model each feature observed in the Fourier transform separately with its own individual path, and having obtained suitable single peak (or "shell" fits), then fitting the spectrum as a whole using parameters generated from the single-shell fitting results. For both Hg and Zn, the feature representing the nearest-neighboring atomic shell was first fit to obtain values for oxygen neighbor coordination number (CN), interatomic bond distance (R) and energy shift (E_0). The E_0 value obtained from fitting the first shell was subsequently used for all further shell fitting. The amplitude reduction factor (S_0^2) for all shells was fixed at 0.9 for Hg and 0.81 for Zn. The S_0^2 for the Hg samples was based on our previous EXAFS fitting in which S_0^2 was allowed to drift for well-characterized crystalline model compounds [18, 40]. The Zn S_0^2 was determined by first obtaining seed values for all other parameters and allowing S_0^2 to float, resulting in a S_0^2

value within the range of values (0.71-0.9) used in other studies [19, 41-46]. The factor σ^2, which serves as a type of Debye-Waller factor and represents the measure of disorder around the atom of interest, was generally allowed to float when fitting the first shell but was fixed at values consistent with those of sorption complexes for second and third shells (0.01 $Å^2$) as determined by our own studies and those of other experimenters in which the Debye-Waller factor for these distant features was allowed to float, typically resulting in σ^2 values of 0.01 $Å^2$ [18, 40]. To improve fitting of the Hg(II) data, which suffered from lower quality, σ^2 was floated for each shell, then fixed at its optimum value of either 0.005 or 0.007 $Å^2$ when fitting subsequent shells.

Generally, coordination numbers generated from such fitting methods are considered to be accurate within ±15%-30% of their reported values [41, 43-47]; however, fixing the σ^2 parameter during the fits artificially reduces the errors associated with coordination numbers as the two variables are correlated. In order to obtain a more accurate representation of the uncertainties in the reported coordination numbers, each fit was separately conducted with σ^2 allowed to float and the resulting errors in the coordination numbers transferred to those of the fitting results where σ^2 was fixed.

3. Results

3.1 Macroscopic uptake

Macroscopic uptake results for all metal(loid)s as a function of aging time are shown in Figure 1. At the earliest sampling point (representing 0 hrs of uptake at elevated temperature), As(V) and Cu(II) are already completely removed from solution while Hg(II) and Zn(II) exhibit considerably lower initial uptake onto the nanoparticles, with approximately 15 μmol/g and 40 μmol/g of the metal removed from solution,

respectively. As the samples are allowed to age for longer periods of time, progressive uptake of Hg(II) and Zn(II) onto/into the iron oxyhydroxide nanoparticles is observed; by the end of 4 days of aging approximately 50% (60 μmol/g) of the Hg(II) has been removed (~85% by the end of 7 days; data not shown) and ~90% (100 μmol/g) of Zn(II) has been removed. Uptake of As(V) and Cu(II) remains essentially complete over the same aging period. Overall, the extent of uptake of each metal(loid) is ordered as follows: As(V)≈Cu(II)>Zn(II)>Hg(II).

Tracking the pH of the reacting suspensions (Figure 2) shows an initial drop in pH within the first 8 hours followed by an upward drift in pH with time for the remainder of the experiment. This is thought to influence the observed macroscopic uptake behavior of the different metal(loid)s and is discussed in more detail in the discussion section.

Measured concentrations of Fe(III) in all supernatants were uniformly low, corresponding to <0.5% of the total iron initially introduced in the form of nanogoethite. This excludes nanoparticle dissolution or passage of suspended nanoparticles through the filters during the filtration step as significant factors and supports the conclusion that the supernatant metal(loid) concentrations accurately reflect the unsorbed fraction of the specific metal(loid).

3.2 Synchrotron X-Ray Microdiffraction

Figure 3 displays μXRD stack plots of the nanogoethite solids aged in the presence of Hg(II), Zn(II), Cu(II), and As(V) (Figures 3a, 3b, 3d, 3e) as well as those aged in the absence of any metals (Figure 3c). The latter samples (referred to from this point forward as the "control" samples) exhibit a clear trend wherein the diffraction patterns become more resolved and individual peaks more distinct with subsequent aging.

These peaks correspond directly to those of goethite as shown by the agreement with the μXRD pattern of the macroscale goethite and the dissimilarity with that of the synthesized ferrihydrite (Figure 4). There is no evidence for shifting of peaks or the appearance of new peaks with aging, implying that no significant compositional change or phase transformation takes place, and hence that the particles remain as goethite throughout the aging process. This is consistent with our previous observations during the aging of goethite nanoparticles from 0-25 days [24], although subtle surface rearrangements may be occurring within the first 24 hours that affect the surface structure yet do not appear to have a significant influence on the metal(loid) uptake trends. Our previous XRD and Fe K-edge EXAFS studies [24] also concluded that this continuous increase in structural ordering as a function of aging was observed as a result of a greater proportion of Fe atoms being associated with the bulk as compared to surface-terminated Fe atoms. Correspondingly, the evolution in the diffraction patterns can be attributed to increasing particle/aggregate size and structural ordering as a result of aggregation-based nanoparticle growth as documented previously through TEM and SAXS/WAXS analysis [24, 29]**.**

Comparison of the diffraction patterns collected from nanoparticles aged in the presence of metal(loid)s with those of the control samples reveals relatively minimal differences for samples aged in the presence of Hg(II) and Zn(II), indicating that the presence or the uptake behavior of these two metals during the aging process does not significantly impede the growth process of the goethite nanoparticles. In contrast, differences can be clearly observed between the control samples and samples aged in the presence of As(V) and Cu(II). Specifically, the improved peak intensity and definition

observed with progressive aging in the control samples is considerably lessened for the As(V)- and Cu(II)-bearing samples, suggesting a retardation of the nanoparticle growth process due to the presence of these metal(loid)s. A similar effect was seen for the uptake of arsenate onto ferrihydrite [48] and was further extensively characterized in Waychunas *et al.* [49].

Integrated area ratios of the 001 peak region to the area of the entire diffraction pattern (A_{001} /A_{total}) as a function of time are plotted for all samples in Figure 5. This peak ratio, used here as a proxy for particle size, generally increases in a sigmoidal growth pattern (as indicated with best-fit third-order polynomial functions) with inflection points at ~48 hours for all samples except those containing As(V), where particle size appears to decline after about 32 hours of aging. This is supported by re-examining the μXRD patterns generated in the presence of As(V), where the overall intensity and peak resolution decrease among patterns with >32 hours aging (Figure 3e). By considering both the μXRD stack plots as well as the peak ratios, the introduced metal(loid)s appear to inhibit the aggregation-based growth of the goethite nanoparticles to different extents, ordered as follows: As(V)>Cu(II)>Zn(II)>Hg(II). This is in direct agreement with the uptake behavior of the metal(loid)s as characterized by ICP-OES analysis. During the later stages of aging there is evidence for a possible acceleration of particle growth in the presence of Hg(II) and Zn(II) relative to the other metal(loid)s and possibly even the control, although data is sparse in this region. This is also consistent with the aforementioned difference in uptake behavior between the metal(loid)s.

3.3 X-Ray Absorption Spectroscopy

Based on the macroscopic uptake data, samples exposed to As(V) and Cu(II) were not anticipated to demonstrate considerable change in metal(loid) speciation with time [48, 50, 51]. This was corroborated by earlier EXAFS investigations of 0, 1, and 5-day aged samples exposed to As(V) and Cu(II) which did not exhibit significant differences between their EXAFS spectra over time (data not shown). As samples exposed to Zn(II) (Γ= 39.7-99.8 μmol/g) and Hg(II) (Γ= 15.7-84.7 μmol/g) in this study showed measurable changes in macroscopic uptake during the course of the experiment, the potential for changes in speciation with time was considerably greater and so EXAFS analysis was focused on these two systems.

Normalized zinc K-edge X-ray absorption near-edge structure (XANES) spectra of selected Zn(II)-sorbed nanogoethite samples are shown in Figure 6. Two distinct edge features can be observed in the XANES spectra: an initial peak at 9665 eV and a second peak at 9668 eV. Simulated XANES spectra calculated by Waychunas *et al.* using model spinel clusters [52] resulted in two similar peaks, with the second peak attributed to a greater number of second-nearest neighbor Fe atoms around the central absorbing Zn atom.

Changes in the coordination of Zn with increased aging are corroborated by the EXAFS spectra and associated Fourier transforms of the same samples (Figure 7), with the latter (representing radial distribution functions that indicate the distance(s) between a central absorbing Zn atom and its nearest-neighboring atoms) showing a clear increase in amplitude with time at distances consistent with second-nearest neighbors (Figure 7b). Quantitative fitting of these features (Table 1) reveals both a Zn-Fe scattering interaction at 3.44±0.03 Å which increases in coordination number after 8 hours of aging as well as

the appearance of a second Zn-Fe feature at 2.99±0.02 Å at 8 hours of aging which increases slightly in coordination by the end of the aging period. Qualitative changes in the EXAFS spectra appear to track these increases in coordination as well (Figure 7a). The shortest, first-neighbor scattering interaction was fitted for all samples with a Zn-O scattering path at an interatomic distance of 1.98±0.02 Å and coordination numbers of ~4 indicating tetrahedral coordination, consistent with other studies which predict that octahedrally coordinated aqueous Zn(II) is typically converted to a tetrahedrally-coordinated species upon sorption to different metal oxide phases [19, 43, 52-55]. However, at sufficiently low sorption densities Zn species have been shown to retain their octahedral hydration shell upon sorption to goethite [56].

Using the parameters generated through EXAFS fitting analysis, potential sorption geometries of Zn(II) onto nanogoethite were modeled using the Spartan '04 molecular modeling program [57]. These models associate the two Zn-Fe distances of 3.44 Å and 2.99 Å most closely with a binuclear bidentate corner-sharing (Figure 8) and mononuclear bidentate edge-sharing (Figure 9) inner-sphere surface sorption complex, respectively. These findings are in agreement with other Zn-iron oxide studies, with the first shell being fit with ~4 O atoms at a atomic distance of 1.97Å and the second shell fit with Fe/Zn at a distance of 3.44-3.51Å (representing corner-sharing bidentate complexes) [19, 43, 45]. The shorter Zn-Fe distance again appears to be consistent with either edge-sharing complexes or a surface precipitate, although the latter is unlikely at the relatively low surface coverages measured.

Mercury L_{III}-edge EXAFS spectra and associated Fourier transforms of selected Hg(II)-sorbed nanogoethite samples are shown in Figure 10. Due to lower total amounts

of uptake on these samples (see Figure 1), their EXAFS spectra are of poorer quality than those featuring Zn(II) uptake. Nevertheless, clear trends in both the EXAFS spectra and Fourier transforms can be observed, specifically an increase in the first Fourier transform feature (generally corresponding to lower frequency k-space EXAFS oscillations) and a concomitant decrease in the more distant Fourier transform feature (generally corresponding to higher frequency k-space EXAFS oscillations). EXAFS fitting analysis (Table 2) identifies these two features as an Hg-O scattering path at 2.06±0.03Å and a Hg-Hg scattering path at 2.53±0.03Å, respectively. Attempts to fit either peak with a Hg-Fe scattering path resulted in a much poorer quality of fit, while inclusion of the same path with the Hg-O and Hg-Hg interactions did not substantially improve the quality of the fit; thus, Hg-Fe scattering paths did not merit inclusion in the final fit results presented. The coordination numbers determined from EXAFS fitting follow the trends observed qualitatively in the Fourier transforms, with the Hg-O coordination increasing from 0.6 to 1.8 and the Hg-Hg coordination decreasing from 0.9 to 0.3 with progressive aging. Coordination numbers less than one are consistent with only a minor fraction of Hg in the sample present in that coordination environment.

The increase in the Hg-O coordination number indicates a progressive tendency towards inner-sphere adsorption as observed in other studies [18]; although the data quality is not sufficient to identify any weaker second-neighbor scattering components such as Fe, the first-shell fitting results likely support the formation of bidentate corner-sharing surface complexes as observed by Collins *et al.* and Kim *et al.* in similar Hg(II)-goethite sorption systems [18, 20]. The Hg-Hg interatomic distance determined from EXAFS fitting is consistent with Hg(I)-Hg(I) distances, which average 2.43-2.69 Å [58,

59] (e.g. Hg_2Cl_2) and implies some degree of photoreduction resulting from exposure to synchrotron radiation. Our earlier studies [18] identified similar Hg-Hg distances for Hg(II)-γ-alumina sorption samples and attributed them to the photoinduced reduction of loosely-sorbed or unsorbed free Hg(II) to the mercurous ion Hg (I), which is known to form dimeric complexes such as the $Hg_2(OH)_2$ aqueous species (Figure 11) [57]. Therefore the presence of Hg-Hg scattering interactions can be taken to represent the fraction of Hg(II) that is weakly associated, perhaps via outer-sphere sorption with the substrate surface, and indicates that poorly sorbed Hg(II) is considerably more susceptible to photoreduction than inner-sphere-sorbed Hg(II).

4. Discussion

This study verifies our proposed hypotheses correlating the effects of progressive metal(loid) uptake with changes in the speciation of the sorbed metal(loid) and predicting that such uptake would have a measurable impact on nanoparticle growth rates. It also identified clear metal(loid)-dependent differences in uptake behavior that additionally influence speciation mode and effects on nanoparticle growth. Such outcomes demonstrate the utility of combining macroscopic uptake experiments, which track the total extent of metal(loid) sorbed to a given geologically-relevant sorbent, with X-ray synchrotron-based methods which allow detailed characterization of both the sorbent and the sorbate as uptake is progressing. A synthesis of complementary techniques is of particular benefit when the sorbent itself, in this case a suspension of nanoscale iron oxyhydroxide particles, is undergoing substantial changes (i.e. aggregation-based growth) during the sorption process. Considerable agreement among the results of the different

methods indicates that variations in the rate and extent of macroscopic uptake as a function of the specific sorbing metal(loid) correspond with effects on particle growth as well as on the mode(s) of metal complexation.

A fundamental difference in sorption behavior as a function of the metal(loid) introduced was apparent in this study, with As(V) and Cu(II) displaying immediate and total uptake while Hg(II) and Zn(II) demonstrated initially low uptake but progressively more uptake with aging. These differences are likely to be in part a result of the metal(loid)-specific uptake dependence on pH to the Fe-oxyhydroxide nanoparticle sorbent. That is, the pH at which the experiments were begun (6.0±0.1) was sufficient to yield maximum uptake of As(V) and Cu(II) but only partial uptake of Hg(II) and Zn(II). Along the standard macroscopic uptake curves for each metal(loid), this would be akin to the top of the curves for the former species and somewhere along the curve for the latter species [60, 61]. For those metal cations not yet at their maximum uptake levels (i.e. Hg(II) and Zn(II), then, the continuous pH increase for all supernatants shown in Figure 2 induces progressive metal uptake as shown directly in the case of Hg(II) (Figure 12).

This early decrease in pH is attributed to re-equilibration through protonation of the substrate surface following base titration to the initial experimental pH; although metal cation adsorption could be a source of proton release to solution [62], the pH drop is also observed in the control experiment where no metal was introduced, precluding the likelihood of cation adsorption as the primary factor in the initial decline in pH. Such an initial decline in pH would also be consistent with a transformation of ferrihydrite to goethite, resulting in the loss of protons to solution. The subsequent increase in pH over time, also observed by Subramaniam and Yiacoumi for the uptake of copper onto ferric

oxide [7], could be attributed either to the slight dissolution of the solid, thus releasing hydroxyl species to solution, or perhaps to particle growth, as the loss of surface area through aggregation could result in a net dehydroxylation effect that increases pH and, correspondingly, the uptake of Hg(II) and Zn(II). Although such a process has yet to be conclusively proven, a schematic reaction involving the bonding of two Fe octahedra and subsequent release of hydroxyls might follow a path similar to the following:

(1) $Fe(O,OH)_6 + Fe(O,OH)_6 \rightarrow Fe_2(O,OH)_{10} + 2OH^-$

The differences in uptake rate as controlled by the varying pH-dependent uptake behaviors of the selected metal(loid)s are clearly reflected in the μXRD results, with those species exhibiting slower, progressive uptake (Hg(II) and Zn(II)) exhibiting minimal to moderate effects on the particle growth process while those featuring rapid uptake (As(V) and Cu(II)) having an immediate and more significant impact on growth. The extent to which the sorption of the specific metal(loid) impedes growth correlates directly with the extent of uptake is shown when comparing the μXRD peak ratio data and the macroscopic uptake data, with the general ordering as follows: As(II)≥Cu(II)>Zn(II)>Hg(II). The trends of particle growth based upon the peak ratio measurements remain roughly the same among the different systems, with a sigmoidal shape suggesting two separate stages of growth or recrystallization. This is not to suggest that only a single mechanism is responsible for growth at any given time; in fact, multiple processes—aggregation-based growth, ripening, surface restructuring/recrystallization—are likely taking place in various proportions throughout the aging experiments. However, the shape of the peak ratios suggests that there is a transition between two dominant growth mechanisms that occurs in the presence of all metal(loid)s studied in

addition to the control. This would agree with our previous studies suggesting that the aggregation-based growth of nanoparticles takes place in the early stages of growth, at which point more traditional ripening-based growth mechanisms dominate the growth process [24].

The effects of rapid metal(loid) uptake on nanoparticle aggregation and growth suggests that surface passivation (site deactivation/poisoning), either through modification of surface charge or alteration of the surface structure/composition, inhibits growth processes during aging, as has been observed and/or predicted with other aqueous species including arsenate, silicate, and other oxyanions [48, 63-65]. Classical growth is likely restricted by reduction of active attachment sites for new atoms, e.g. reduction in "kink" or "edge" sites. The effect ought to be related to the strength and hence stability of such complexation reactions. In the case of aggregation, while some degree of aggregation may still occur, the process is reduced due to the presence of metal impurities on aggregation interfaces which would need to be desorbed or incorporated to allow aggregation to proceed. The latter effect could result in aggregated particles with poor overall structural coherence, and hence XRD patterns that do not show improved crystallization (internal order). In systems where metal uptake is initially low and further uptake occurs over time, nanoparticle growth is still impeded but at a considerably lesser rate. This direct apparent relationship between the extent of metal(loid) uptake and the rate of particle growth supports the persistence of nanoscale and/or less structured/amorphous mineral phases in natural systems, where any number of aqueous ligands in addition to metal ions present in natural waters may similarly sorb to and passivate such particle surfaces.

The progressive metal adsorption observed in the Hg(II) and Zn(II) systems allows the observation of real-time transitions between distinct modes of uptake using the atomic-scale probe of EXAFS spectroscopy. In surface complexation models [4], sorption is often characterized as a two-step process, with metals first binding to the most high-energy sorption sites first; once these sites are saturated yet conditions for further sorption are still favorable, higher surface loading levels are achieved by continued sorption to lower-energy sorption sites.

This appears to be taking place in the case of Zn(II), where inner-sphere bidentate corner-sharing surface complexes are initially formed, followed later by inner-sphere bidentate edge-sharing surface complexes. These results are consistent with other studies [18, 19, 65-68] that find bidentate corner-sharing surface species as a preferred mode of metal complexation in a number of metal sorption systems. As sites where such species are likely to form tend to be concentrated at the edges, steps, and defects of a mineral surface, which typically feature undercoordinated oxygen atoms in the $Fe(O,OH)_6$ octahedra that form the building blocks of iron oxyhydroxide phases, it follows that these sites will serve as high-energy locations for the initial rapid stages of metal sorption. Once these sites are saturated, a second mode of Zn(II) sorption comprised of edge-sharing surface complexes appears to dominate for the duration of the experiment, representing an additional and increasing proportion of the macroscopic uptake observed from 8 hours of aging onwards. While nanosized Zn-Fe precipitates cannot be conclusively ruled out, the relatively low surface coverages exhibited throughout the experiment suggest direct chemical sorption as the primary means of uptake.

Although less clear, progressive changes in the mode of Hg(II) uptake appear to be occurring as well, with the initial formation of loosely-bound, potentially outer-sphere Hg(II) surface complexes which are easily converted through beam photoreduction into Hg(I) dimers. With continued aging, however, there appears to be an increased preference for inner-sphere surface complexation, evidenced by the relatively short Hg-O distances consistent with direct binding to the surface and a reduced degree of Hg(II) photoreduction resulting in lower Hg-Hg coordination numbers.

5. Conclusions

The work presented in this study provides substantial evidence indicating that metal(loid) uptake onto iron oxyhydroxide nanoparticles either is instantaneous or increases progressively with continued aging/growth of the particles at elevated temperatures. At the same time, such uptake serves to inhibit particle growth, likely through surface passivation effects. In systems where the process of metal uptake occurs simultaneously and continuously with particle growth, as observed from the macroscopic uptake data, a proportion of the initially-sorbed metal will inevitably be located at particle interfaces that can later join as the particles aggregate. Since the macroscopic data shows that nanoparticle growth in the presence of Hg(II) and Zn(II) does not result in a net desorption of metal from the surface, but rather occurs alongside increasing macroscopic uptake, it is likely that some of the metal that is initially sorbed onto nanoparticle surfaces exposed directly to solution becomes incorporated into aggregation zones connecting particles and eventually the larger aggregates' bulk structure with time. The speciation of Zn(II) and Hg(II) at the greatest aging times, as determined in this study by EXAFS

spectroscopy, may represent a point along the continuum between surface-sorbed and structurally incorporated metals. A deeper level of sequestration as would be implied by such structural incorporation would presumably restrict metal re-mobilization into solution and lessen the potential environmental impacts of such metals by retaining them more fixedly in the solid phase.

Further evidence for the structural incorporation of metal(loid)s through simultaneous sorption and nanoparticle aggregation could be obtained macroscopically by conducting desorption experiments to gauge the relative extent of metals that can be released at different stages of aggregation and spectroscopically by identifying evidence of metal(loid) (co)-precipitation with or incorporation into the nanoparticle substrate. For example, an increase in Zn-Fe coordination numbers beyond that predicted for the surface sorption complexes proposed would indicate a higher degree of Fe coordination around the average Zn atom [45], as would be the case for zinc that has become structurally incorporated into the nanoparticle bulk region. Identification of the geochemical and aging conditions that maximize such methods of metal removal from solution would help more permanently entrain metals in the solid phase and hold implications for the effective remediation of metal-contaminated waters.

Acknowledgements - We wish to acknowledge the invaluable staff support at the ALS (Nobumichi Tamura, Bryan Valek) and SSRL (John Bargar, Joe Rogers, Sam Webb) for their assistance with μXRD and EXAFS data collection, respectively. We also thank Guangchou Li at Stanford University for help with ICP-OES measurements. Finally, we would like to thank Kim Environmental Geochemistry group members Lauryn DeGreeff, Brian Reinsch, and Henry Yan for their help with sample preparation and laboratory experimentation. The insightful comments of editor M. Barnett and two anonymous reviewers contributed greatly to the improvement of the manuscript. The Advanced Light Source is supported by the Director, Office of Science, Office of Basic Energy Sciences, of the U.S. Department of Energy under Contract No. DE-AC02-05CH11231. Portions of this research were carried out at the Stanford Synchrotron Radiation

Laboratory, a national user facility operated by Stanford University on behalf of the U.S. Department of Energy, Office of Basic Energy Sciences. This study was supported by the Wilkinson College of Letters and Sciences, Chapman University, and a grant from the American Chemical Society – Petroleum Research Grant, PRF # 44721-GB10.

References

1. Ford, R.G., A.C. Scheinost, and D.L. Sparks, *Frontiers in metal sorption/precipitation mechanisms on soil mineral surfaces*, in *Advances in Agronomy, Vol 74*. 2001. p. 41-62.
2. Scheidegger, A.M. and D.L. Sparks, *A critical assessment of sorption-desorption mechanisms at the soil mineral/water interface.* Soil Science, 1996. **161**(12): p. 813-831.
3. Sposito, G., *The Surface Chemistry of Soils*. 1st ed. 1984, New York: Oxford University Press. 234.
4. Dzomback, D.A. and F.M.M. Morel, *Surface Complexation Modeling: Hydrous Ferric Oxide*. 1990, New York, NY: John Wiley & Sons. 393.
5. Trivedi, P. and L. Axe, *A comparison of strontium sorption to hydrous aluminum, iron, and manganese oxides.* Journal of Colloid and Interface Science, 1999. **218**(2): p. 554-563.
6. Axe, L. and A.J. Anderson, *Intraparticle Diffusion of Metal Contaminants in Amorphous Oxide Minerals*, in *Adsorption of Metals by Geomedia* E.A. Jenne, Editor. 1998, Academic Press: San Diego p. 193-205.
7. Subramaniam, K. and S. Yiacoumi, *Modeling kinetics of copper uptake by inorganic colloids under high surface coverage conditions.* Colloids and Surfaces a-Physicochemical and Engineering Aspects, 2001. **191**(1-2): p. 145-159.
8. Scheidegger, A.M., G.M. Lamble, and D.L. Sparks, *Spectroscopic evidence for the formation of mixed-cation hydroxide phases upon metal sorption on clays and aluminum oxides.* Journal of Colloid and Interface Science, 1997. **186**(1): p. 118-128.
9. Dzombak, D.A. and F.M.M. Morel, *Sorption of Cadmium on Hydrous Ferric Oxide at High Sorbate/Sorbent Ratios: Equalibrium, Kinetics, and Modeling.* Journal of Colloid & Interface Science, 1986. **112**(2): p. 588-598.
10. Egirani, D.E., A.R. Baker, and J.E. Andrews, *Copper and zinc removal from aqueous solution by mixed mineral systems I. Reactivity and removal kinetics.* Journal of Colloid and Interface Science, 2005. **291**(2): p. 319-325.
11. Dyer, J.A., P. Trivedi, N.C. Scrivner, and D.L. Sparks, *Surface complexation modeling of zinc sorption onto ferrihydrite.* Journal of Colloid and Interface Science, 2004. **270**(1): p. 56-65.
12. Villalobos, M., M.A. Trotz, and J.O. Leckie, *Surface complexation modeling of carbonate effects on the adsorption of Cr(VI), Pb(II), and U(VI) on goethite.* Environmental Science & Technology, 2001. **35**(19): p. 3849-3856.
13. Trivedi, P. and L. Axe, *Ni and Zn sorption to amorphous versus crystalline iron oxides: Macroscopic studies.* Journal of Colloid and Interface Science, 2001. **244**(2): p. 221-229.

14. Farquhar, M.L., J.M. Charnock, F.R. Livens, and D.J. Vaughan, *Mechanisms of arsenic uptake from aqueous solution by interaction with goethite, lepidocrocite, mackinawite, and pyrite: An X-ray absorption spectroscopy study.* Environmental Science & Technology, 2002. **36**(8): p. 1757-1762.
15. Foster, A.L., G.E. Brown, and G.A. Parks, *X-ray absorption fine structure study of As(V) and Se(IV) sorption complexes on hydrous Mn oxides.* Geochimica Et Cosmochimica Acta, 2003. **67**(11): p. 1937-1953.
16. Fendorf, S., M.J. Eick, P. Grossl, and D.L. Sparks, *Arsenate and chromate retention mechanisms on goethite .1. Surface structure.* Environmental Science & Technology, 1997. **31**(2): p. 315-320.
17. Morton, J.D., J.D. Semrau, and K.F. Hayes, *An X-ray absorption spectroscopy study of the structure and reversibility of copper adsorbed to montmorillonite clay.* Geochimica et Cosmochimica Acta, 2001. **65**(16): p. 2709-2722.
18. Kim, C.S., J.J. Rytuba, and G.E. Brown, Jr., *EXAFS study of mercury(II) sorption to Fe- and Al-(hydr)oxides: I. Effects of pH.* Journal of Colloid and Interface Science, 2004. **271**: p. 1-15.
19. Trivedi, P., J.A. Dyer, D.L. Sparks, and K. Pandya, *Mechanistic and thermodynamic interpretations of zinc sorption onto ferrihydrite.* Journal of Colloid and Interface Science, 2004. **270**(1): p. 77-85.
20. Collins, C.R., D.M. Sherman, and K.V. Ragnarsdottir, *Surface complexation of Hg2+ on goethite: Mechanism from EXAFS spectroscopy and density functional calculations.* Journal of Colloid and Interface Science, 1999. **219**(2): p. 345-350.
21. Kersting, A.B., D.W. Efurd, D.L. Finnegan, D.J. Rokop, D.K. Smith, and J.L. Thompson, *Migration of plutonium in ground water at the Nevada Test Site.* Nature, 1999. **397**(6714): p. 56-59.
22. Vilks, P., L.H. Frost, and D.B. Bachinski, *Field-scale colloid migration experiments in a granite fracture.* Journal of Contaminant Hydrology, 1997. **26**(1-4): p. 203-214.
23. Novikov, A.P., S.N. Kalmykov, S. Utsunomiya, R.C. Ewing, F. Horreard, A. Merkulov, S.B. Clark, V.V. Tkachev, and B.F. Myasoedov, *Colloid transport of plutonium in the far-field of the Mayak Production Association, Russia.* Science, 2006. **314**(5799): p. 638-641.
24. Waychunas, G.A., C.S. Kim, and J.F. Banfield, *Nanoparticulate oxide minerals in soils and sediments: unique properties and contaminant scavenging mechanisms.* Journal of Nanoparticle Research, 2005. **7**: p. 409-433.
25. Madden, A.S., M.F. Hochella, and T.P. Luxton, *Insights for size-dependent reactivity of hematite nanomineral surfaces through Cu2+ sorption.* Geochimica Et Cosmochimica Acta, 2006. **70**(16): p. 4095-4104.
26. Jenne, E.A., ed. *Adsoprtion of Metals by Geomedia* Variables, Mechanisms, and Model Applications 1998, Academic Press: San Diego.
27. Redden, G.D., J. Li, and J.O. Leckie, *Adsorption of U^{VI} and citric acid on goethite, gibbsite, and kaolinite: Comparing results for binary and ternary systems.*, in *Adosption of Metals by Geomedia* E.A. Jenne, Editor. 1998, Academic Press: San Diego. p. 292-313.

28. Kinniburgh, D.G., W.H. Van Riemsdijk, L.K. Koopal, and M.F. Benedetti, *Ion binding to humic Substances* in *Adsorption of Metals by Geomedia* E.A. Jenne, Editor. 1998, Academic Press San Diego p. 484-517.
29. Guyodo, Y., A. Mostrom, R.L. Penn, and S.K. Banerjee, *From Nanodots to Nanorods: Oriented aggregation and magnetic evolution of nanocrystalline goethite.* Geophysical Research Letters, 2003. **30**(10): p. 1512.
30. Atkinson, R.J., A.M. Posner, and J.P. Quirk, *Crystal nucleation in Fe(III) solutions and hydroxide gels.* Journal of Inorganic & Nuclear Chemistry, 1968. **30**: p. 2371-2381.
31. Schwertmann, U. and R.M. Cornell, *Iron oxides in the laboratory: preparation and characterization.* 1991, New York, NY: VCH Publishers, Inc. 137.
32. Gilbert, B., G. Lu, and C. Kim, *Stable cluster formation in aqueous suspensions of iron oxyhydroxide nanoparticles.* Journal of Colloid and Interface Science, In Press.
33. Tamura, N. *X-ray Microdiffraction Analysis Software (XMAS).* [cited; Available from: http://xraysweb.lbl.gov/microdif/user_resources.htm.
34. Corporation, O., *Origin*. 2006: Northampton, MA. p. Software analysis program
35. Rakovan, J., U. Becker, and M.F. Hochella, *Aspects of goethite surface microtopography, structure, chemistry, and reactivity.* American Mineralogist, 1999. **84**(5-6): p. 884-894.
36. Waychunas, G.A. and G.E. Brown, Jr., *Fluorescence yield XANES and EXAFS experiments: application to highly dilute and surface samples.* Advances in X-Ray Analysis, 1994. **37**: p. 607-617.
37. Stern, E.A. and S.M. Heald, *X-ray filter assembly for fluorescence measurements of x-ray absorption fine structure.* Review of Scientific Instruments, 1979. **50**(12): p. 1579-1582.
38. Webb, S.M. *Sam's Interface for XAS Package (SixPACK).* [cited; Available from: http://www-ssrl.slac.stanford.edu/~swebb/index.htm.
39. Zabinsky, S.I., J.J. Rehr, A. Ankudinov, R.C. Albers, and M.J. Eller, *Multiple-scattering calculations of X-ray absorption spectra.* Physical Review B, 1995. **52**: p. 2995-3009.
40. Kim, C.S., J.J. Rytuba, and G.E. Brown, Jr., *EXAFS study of mercury(II) sorption to Fe- and Al-(hydr)oxides: II. Effects of chloride and sulfate.* Journal of Colloid and Interface Science, 2004. **270**: p. 9-20.
41. Pan, G., Y.W. Qin, X.L. Li, T.D. Hu, Z.Y. Wu, and Y.N. Xie, *EXAFS studies on adsorption-desorption reversibility at manganese oxides-water interfaces I. Irreversible adsorption of zinc onto manganite (gamma-MnOOH).* Journal of Colloid and Interface Science, 2004. **271**(1): p. 28-34.
42. Grafe, M. and D.L. Sparks, *Kinetics of zinc and arsenate co-sorption at the goethite-water interface.* Geochimica Et Cosmochimica Acta, 2005. **69**(19): p. 4573-4595.
43. Trivedi, P., L. Axe, and T.A. Tyson, *An analysis of zinc sorption to amorphous versus crystalline iron oxides using XAS.* Journal of Colloid and Interface Science, 2001. **244**(2): p. 230-238.

44. Nachtegaal, M. and D.L. Sparks, *Effect of iron oxide coatings on zinc sorption mechanisms at the clay-mineral/water interface.* Journal of Colloid and Interface Science, 2004. **276**(1): p. 13-23.
45. Waychunas, G.A., C.C. Fuller, and J.A. Davis, *Surface complexation and precipitate geometry for aqueous Zn(II) sorption on ferrihydrite I: X-ray absorption extended fine structure spectroscopy analysis.* Geochimica Et Cosmochimica Acta, 2002. **66**(7): p. 1119-1137.
46. Roberts, D.R., R.G. Ford, and D.L. Sparks, *Kinetics and mechanisms of Zn complexation on metal oxides using EXAFS spectroscopy.* Journal of Colloid and Interface Science, 2003. **263**(2): p. 364-376.
47. Grafe, M., M. Nachtegaal, and D.L. Sparks, *Formation of metal-arsenate precipitates at the goethite-water interface.* Environmental Science & Technology, 2004. **38**(24): p. 6561-6570.
48. Waychunas, G.A., B.A. Rea, C.C. Fuller, and J.A. Davis, *Surface chemistry of ferrihydrite: 1. EXAFS studies of the geometry of coprecipitated and adsorbed arsenate.* Geochimica Et Cosmochimica Acta, 1993. **57**(10): p. 2251-2269.
49. Waychunas, G.A., C.C. Fuller, B.A. Rea, and J.A. Davis, *Wide angle X-ray scattering (WAXS) study of "two-line" ferrihydrite structure: Effect of arsenate sorption and counterion variation and comparison with EXAFS results.* Geochimica Et Cosmochimica Acta, 1996. **60**(10): p. 1765-1781.
50. O'Reilly, S.E., D.G. Strawn, and D.L. Sparks, *Residence time effects on arsenate adsorption/desorption mechanisms on goethite.* Soil Science Society of America Journal, 2001. **65**(1): p. 67-77.
51. Manceau, A., *The Mechanism of Anion Adsorption on Iron-Oxides - Evidence for the Bonding of Arsenate Tetrahedra on Free Fe(O,Oh)(6) Edges.* Geochimica Et Cosmochimica Acta, 1995. **59**(17): p. 3647-3653.
52. Waychunas, G.A., C.C. Fuller, J.A. Davis, and J.J. Rehr, *Surface complexation and precipitate geometry for aqueous Zn(II) sorption on ferrihydrite: II. XANES analysis and simulation.* Geochimica Et Cosmochimica Acta, 2003. **67**(5): p. 1031-1043.
53. Lee, S.W. and P.R. Anderson, *EXAFS study of Zn sorption mechanisms on hydrous ferric oxide over extended reaction time.* Journal of Colloid and Interface Science, 2005. **286**(1): p. 82-89.
54. O'Day, P.A., S.A. Carroll, and G.A. Waychunas, *Rock-water interactions controlling zinc, cadmium, and lead concentrations in surface waters and sediments, US Tri-State Mining District. 1. Molecular identification using X-ray absorption spectroscopy.* Environmental Science & Technology, 1998. **32**(7): p. 943-955.
55. Trainor, T.P., G.E. Brown, Jr., and G.A. Parks, *Adsorption and precipitation of aqueous Zn(II) on alumina powders.* Journal of Colloid and Interface Science, 2000. **231**(2): p. 359-372.
56. Schlegel, M.L., A. Manceau, and L. Charlet, *EXAFS study of Zn and ZnEDTA sorption at the goethite (alpha-FeOOH)/water interface.* Journal De Physique Iv, 1997. **7**(C2): p. 823-824.
57. Kong, J., C.A. White, A.I. Krylov, D. Sherrill, R.D. Adamson, T.R. Furlani, M.S. Lee, A.M. Lee, S.R. Gwaltney, T.R. Adams, C. Ochsenfeld, A.T.B. Gilbert, G.S.

Kedziora, V.A. Rassolov, D.R. Maurice, N. Nair, Y.H. Shao, N.A. Besley, P.E. Maslen, J.P. Dombroski, H. Daschel, W.M. Zhang, P.P. Korambath, J. Baker, E.F.C. Byrd, T. Van Voorhis, M. Oumi, S. Hirata, C.P. Hsu, N. Ishikawa, J. Florian, A. Warshel, B.G. Johnson, P.M.W. Gill, M. Head-Gordon, and J.A. Pople, *Q-chem 2.0: A high-performance ab initio electronic structure program package.* Journal of Computational Chemistry, 2000. **21**(16): p. 1532-1548.

58. Grdenic, D. and G. Tunell, *Mercury: Crystal Chemistry.*, in *Handbook of Geochemistry*, K.H. Wedepohl, Editor. 1969, Springer-Verlag: New York, NY. p. 8.
59. Pervukhina, N.V., G.V. Romanenko, S.V. Borisov, S.A. Magarill, and N.A. Palchik, *Crystal chemistry of mercury(I) and mercury(I, II) minerals.* Journal of Structural Chemistry, 1999. **40**(3): p. 461-476.
60. Ponthieu, M., F. Juillot, T. Hiemstra, W.H. van Riemsdijk, and M.F. Benedetti, *Metal ion binding to iron oxides.* Geochimica Et Cosmochimica Acta, 2006. **70**(11): p. 2679-2698.
61. Benjamin, M.M. and J.O. Leckie, *Multiple-Site Adsorption of Cd, Cu, Zn, and Pb on Amorphous Iron Oxyhydroxide.* Journal of Colloid & Interface Science, 1981. **79**(1): p. 209-221.
62. Stumm, W., *Chemistry of the Solid-Water Interface: Processes at the Mineral-Water and Particle-Water Interface in Natural Systems*. 1st ed. 1992, New York, NY: John Wiley & Sons, Inc. 428.
63. Fuller, C.C., J.A. Davis, and G.A. Waychunas, *Surface-Chemistry of Ferrihydrite .2. Kinetics of Arsenate Adsorption and Coprecipitation.* Geochimica Et Cosmochimica Acta, 1993. **57**(10): p. 2271-2282.
64. Myneni, S.C.B., S.J. Traina, T.J. Logan, and G.A. Waychunas, *Oxyanion behavior in alkaline environments: Sorption and desorption of arsenate in ettringite.* Environmental Science & Technology, 1997. **31**(6): p. 1761-1768.
65. Stumm, W., *Reactivity at the mineral-water interface: Dissolution and inhibition.* Colloids and Surfaces a-Physicochemical and Engineering Aspects, 1997. **120**(1-3): p. 143-166.
66. Collins, C.R., K.V. Ragnarsdottir, and D.M. Sherman, *Effect of inorganic and organic ligands on the mechanism of cadmium sorption to goethite.* Geochimica et Cosmochimica Acta, 1999. **63**(19-20): p. 2989-3002.
67. Peacock, C.L. and D.M. Sherman, *Copper(II) sorption onto goethite, hematite and lepidocrocite: A surface complexation model based on ab initio molecular geometries and EXAFS spectroscopy.* Geochimica Et Cosmochimica Acta, 2004. **68**(12): p. 2623-2637.
68. Paktunc, D., A. Foster, S. Heald, and G. Laflamme, *Speciation and characterization of arsenic in gold ores and cyanidation tailings using X-ray absorption spectroscopy.* Geochimica et Cosmochimica Acta, 2004. **68**(5): p. 969-983.

Figures

Figure 1: Macroscopic batch metal(loid) sorption onto nanoscale goethite (4.49 g/L) as a function of aging time. $[Me]_I$ = 0.5 mM, pH = 6, *I* = 0.1$NaNO_3$, T = 78.0°C. Error bars are contained within the data points.

Figure 2: Measured pH values in metal(loid)-nanoparticle solutions as a function of aging. Error bars are contained within the data points.

Figure 3 (a-e): Synchrotron micro-X-ray diffraction (μXRD) patterns for nanoparticles aged in the presence of: a) Zn(II); b) Hg(II) c) no metal (control); d) Cu(II); and e) = As(V). Patterns are oriented in order of decreasing aging time (most aged at top); the time interval between patterns is 8 hours.

Figure 4: Synchrotron X-ray diffraction patterns for synthesized goethite and 2-line ferrihydrite compared with the control at 0 and 96 hours aging.

Figure 5: Ratios of the integrated area of the 001 peak (25° - 32° 2θ) to entire data set (25° - 75° 2θ). Lines are 3rd order polynomial best fits used to track the growth rates of nanoparticles along the primary growth axis of goethite (c-axis). R-factors of fits: Blank= 0.7736; As(V)= 0.8194; Cu(II)= 0.9025; Hg(II)= 0.9482; Zn(II)= 0.8802.

Figure 6: Normalized XANES spectra for Zn(II) sorption onto nanoscale goethite, with arrows and vertical lines pointing out relevant features. The second peak (2) has been correlated to an increase in the number of next-nearest-neighbor Fe atoms based on previous spinel cluster calculations [52].

Figure 7: Fits for a) k^3-weighted Zn(II) K edge EXAFS and b) Fourier transforms of goethite nanoparticle samples aged in the presence of Zn(II) for varying lengths of time. The solid line represents the experimental data and the grey line indicates the best fits.

Figure 8: Simulated corner sharing bonding configuration for Zn onto $Fe(O,OH)_6$ octahedra representing the goethite structure using Spartan Pro. The distance between Zn-Fe is represented by the grey dotted line and was found to be between 3.40-3.41 Å.

Figure 9: Simulated edge sharing bonding configuration for Zn onto $Fe(O,OH)_6$ using Spartan Pro. The distance between Zn and Fe is represented by the grey dotted line and was found to be 2.98 Å.

Figure 10: Fits for a) k^3-weighted Hg(II) L_{III} edge EXAFS and b) Fourier transforms of goethite nanoparticle samples aged in the presence of Hg(II) for varying lengths of time. The solid line represents the experimental data and the grey line indicates the best fits.

Figure 11: Simulated bonding configuration for $Hg_2(OH)_2$ species.

Figure 12: Comparison of percent of mercury uptake and pH as a function of aging. Error bars are contained within the data points.

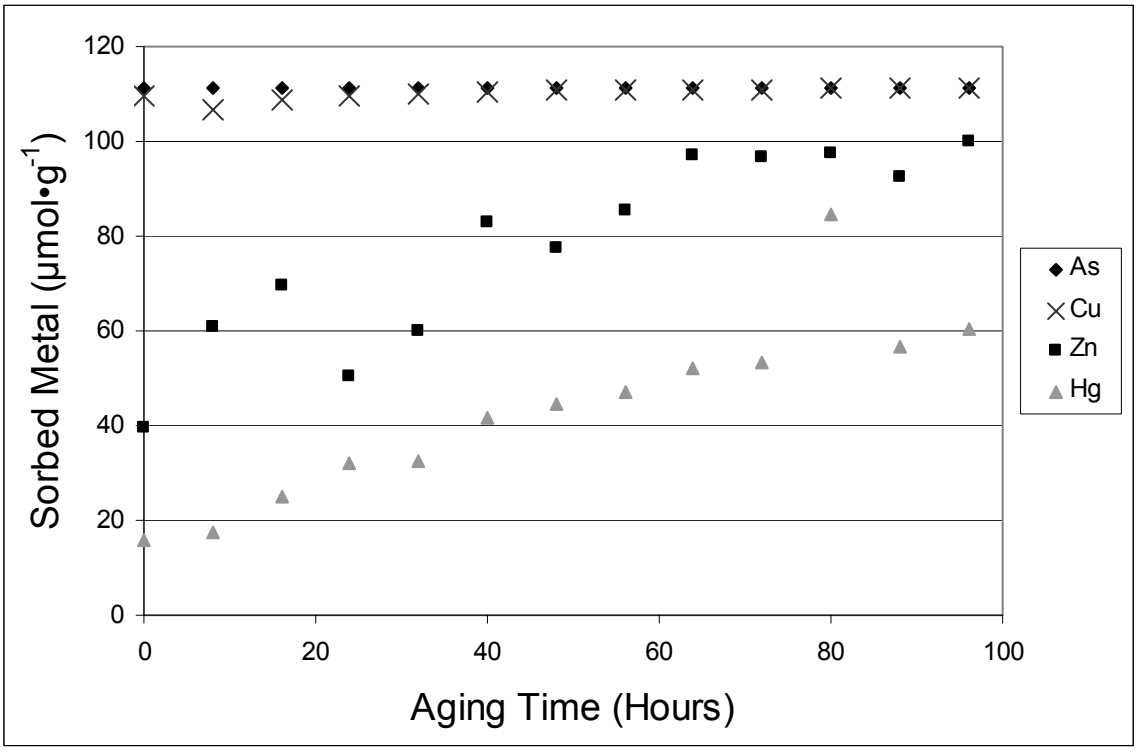
120
100
80
60
40
20
0
Sorbed Metal (µmol•g-1)
0
20
40
60
80
100
Aging Time (Hours)
As
Cu
Zn
Hg

Figure 1

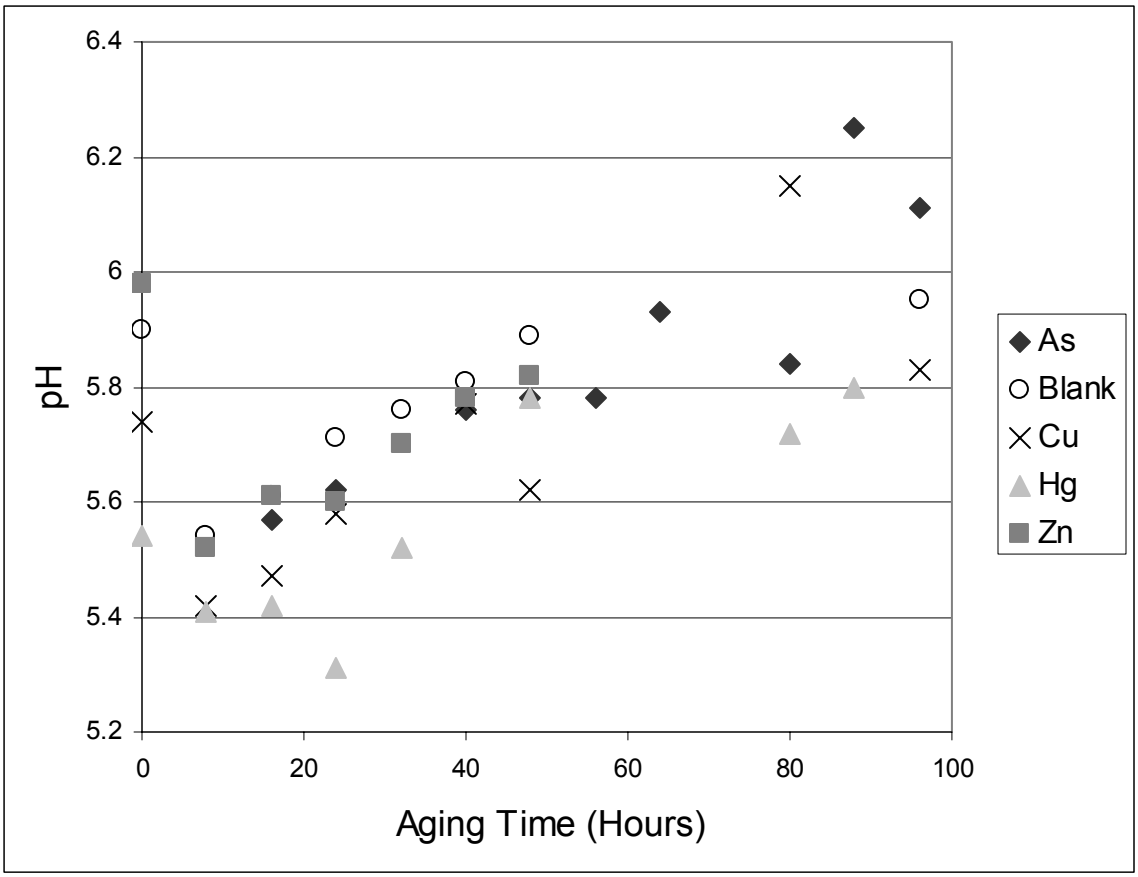
6.4
6.2
6
5.8
5.6
5.4
5.2
pH
0
20
40
60
80
100
Aging Time (Hours)
As
Blank
Cu
Hg
Zn

Figure 2

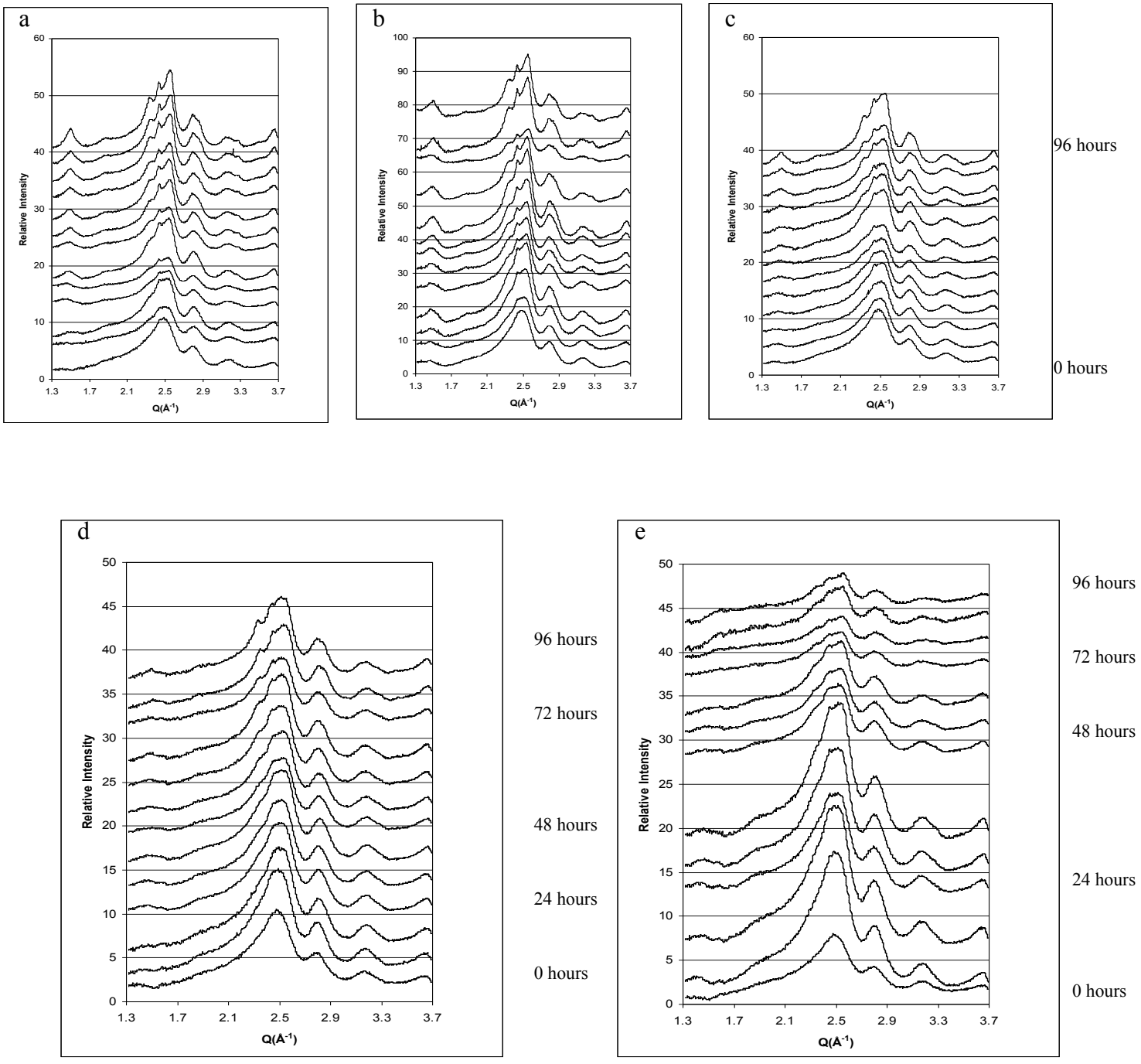
a
b
c
d
e
Relative Intensity
Q(Å⁻¹)
96 hours
72 hours
48 hours
24 hours
0 hours

Figure 3 (a-e)

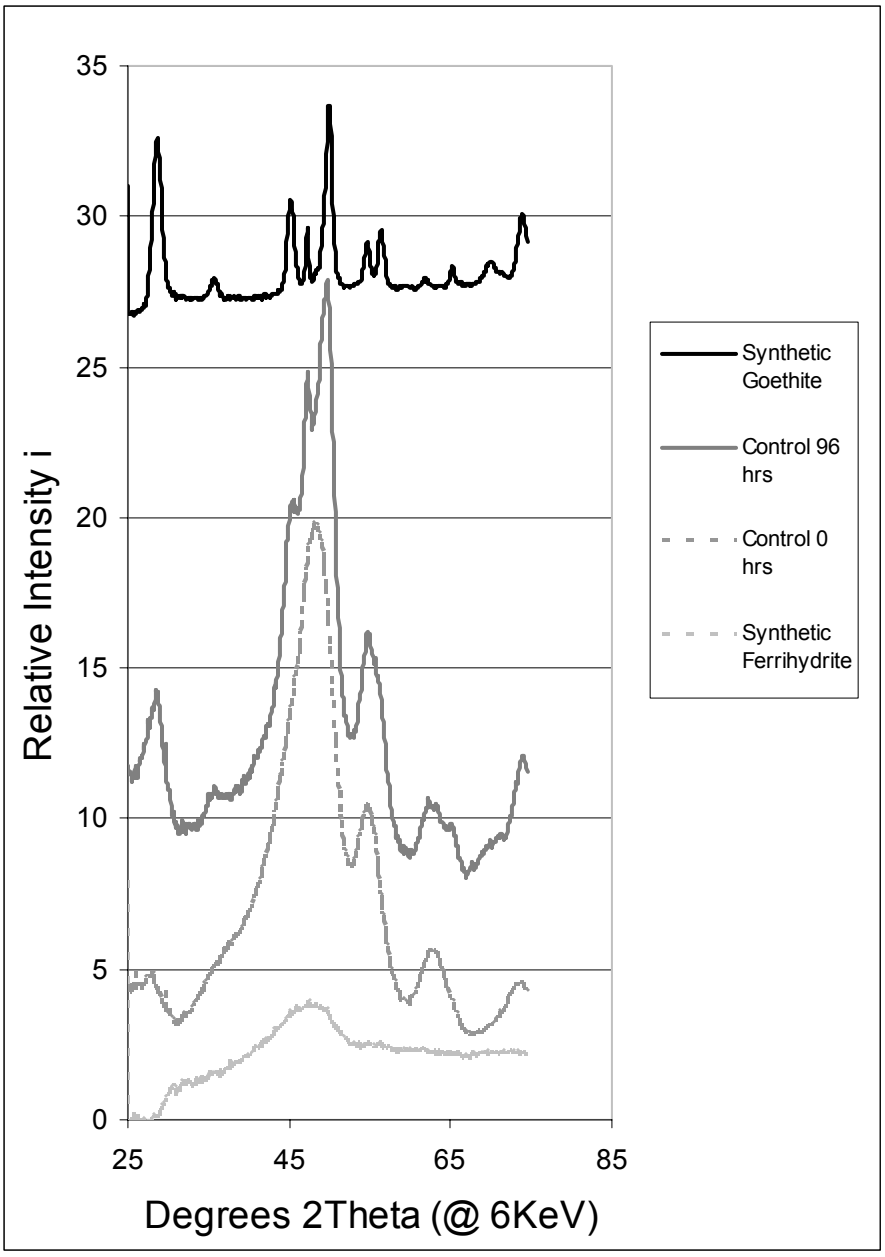
35
30
25
20
15
10
5
0
Relative Intensity i
25
45
65
85
Degrees 2Theta (@ 6KeV)
Synthetic Goethite
Control 96 hrs
Control 0 hrs
Synthetic Ferrihydrite
Figure 4

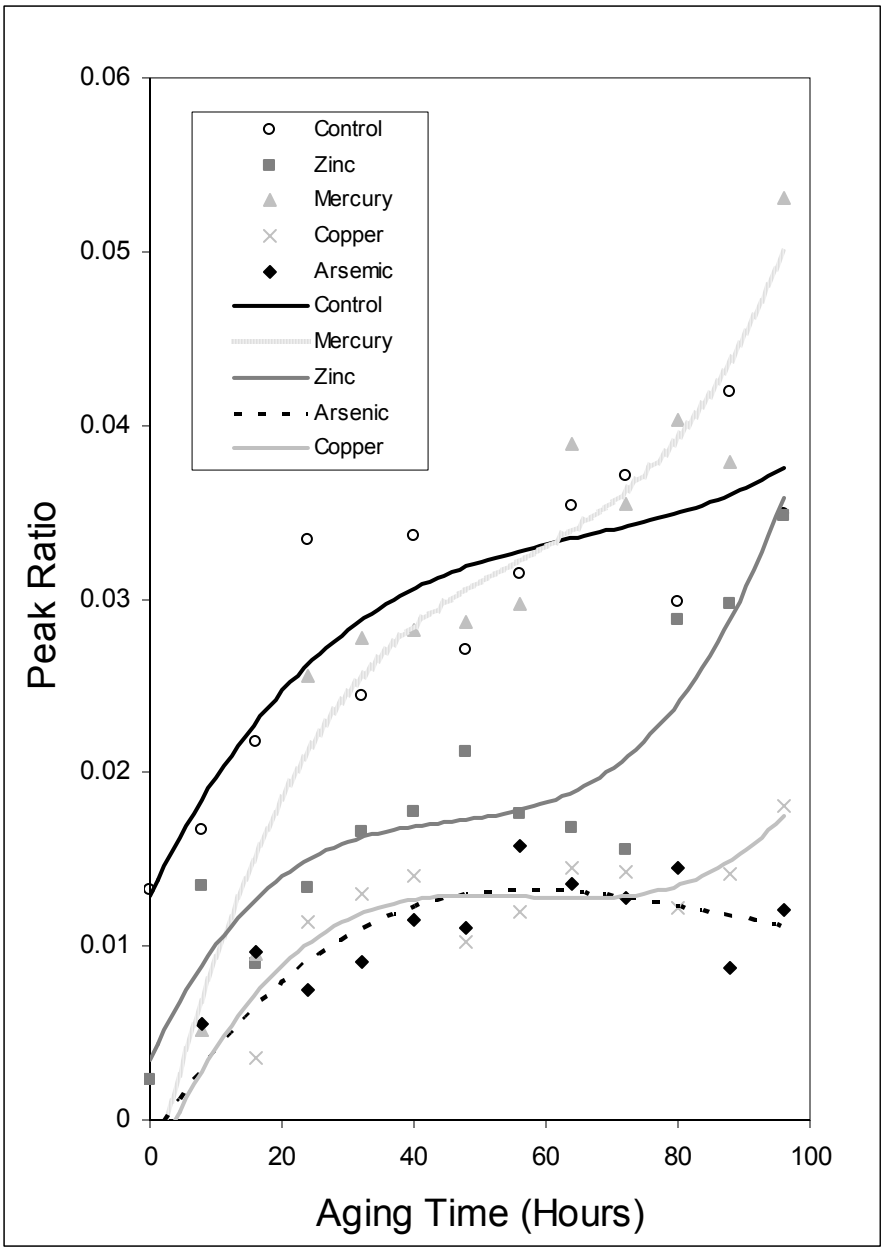
0.06
0.05
0.04
0.03
0.02
0.01
0
Peak Ratio
0
20
40
60
80
100
Aging Time (Hours)
Control
Zinc
Mercury
Copper
Arsemic
Control
Mercury
Zinc
Arsenic
Copper
Figure 5

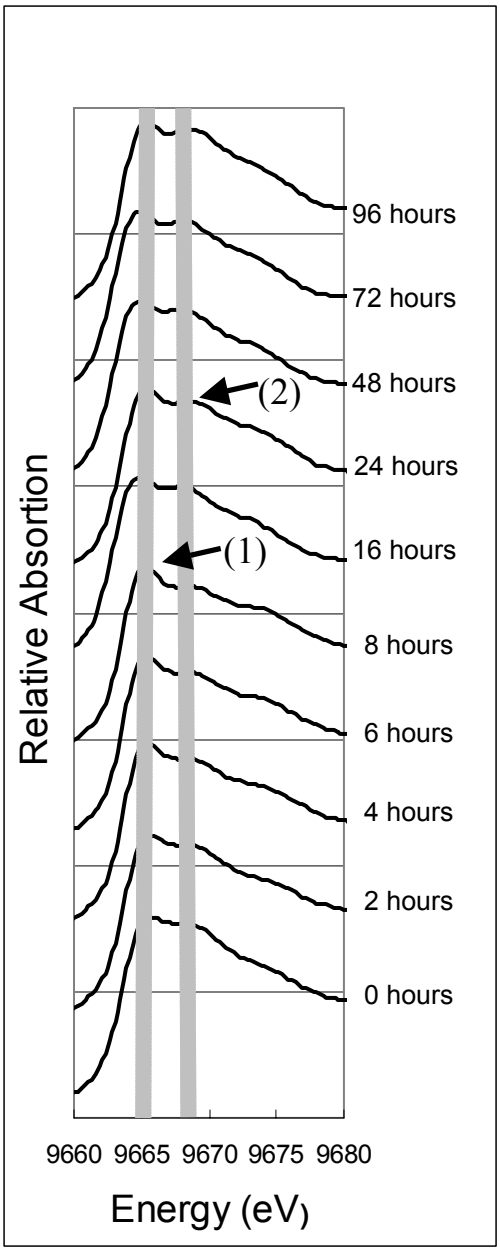
96 hours
72 hours
48 hours
24 hours
16 hours
8 hours
6 hours
4 hours
2 hours
0 hours
(2)
(1)
Relative Absortion
9660 9665 9670 9675 9680
Energy (eV)
Figure 6

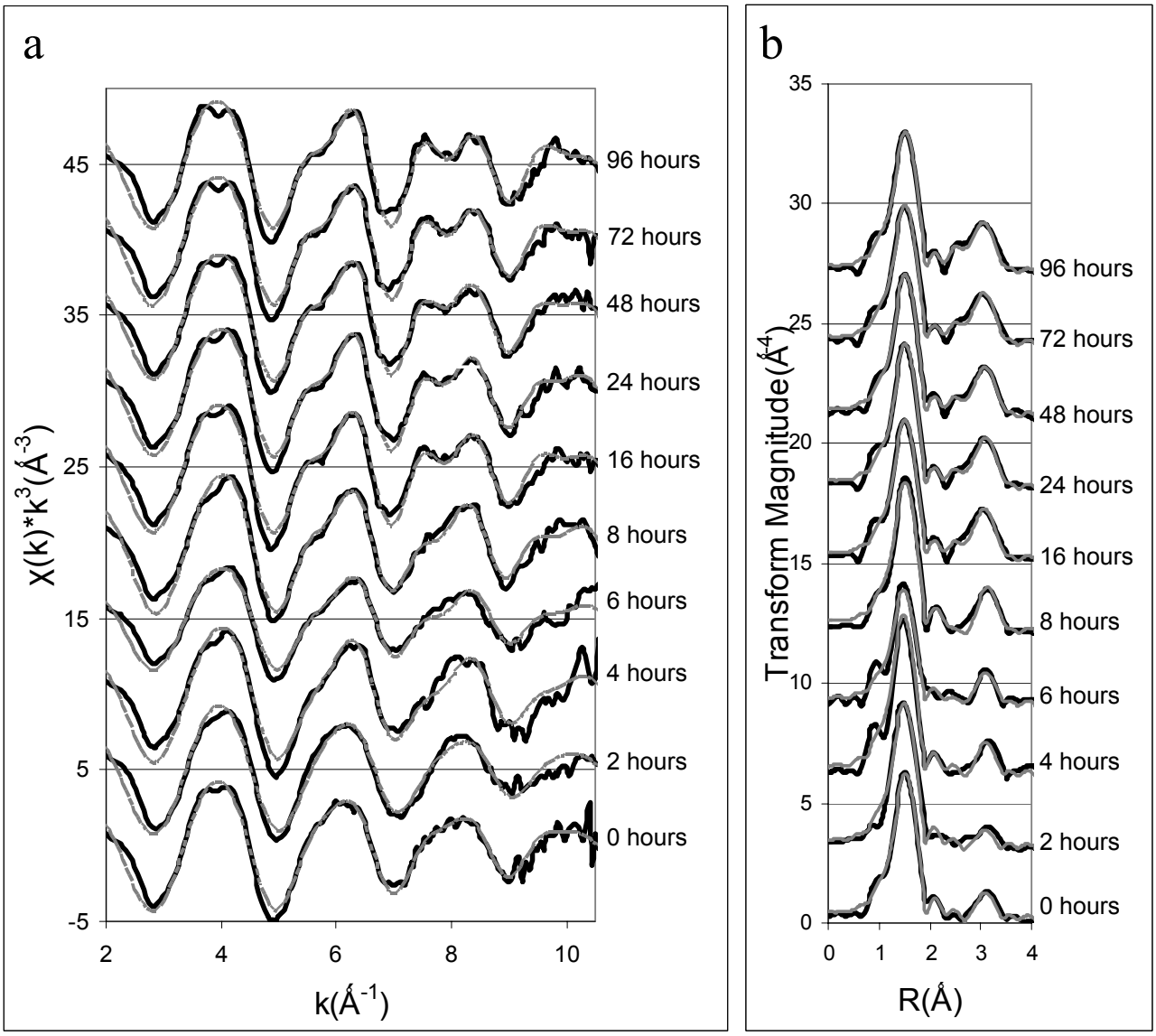
a
45
35
25
15
5
-5
2
4
6
8
10
k(Å-1)
χ(k)*k3(Å-3)
96 hours
72 hours
48 hours
24 hours
16 hours
8 hours
6 hours
4 hours
2 hours
0 hours
b
35
30
25
20
15
10
5
0
0
1
2
3
4
R(Å)
Transform Magnitude(Å-4)
96 hours
72 hours
48 hours
24 hours
16 hours
8 hours
6 hours
4 hours
2 hours
0 hours

Figure 7 (a,b)

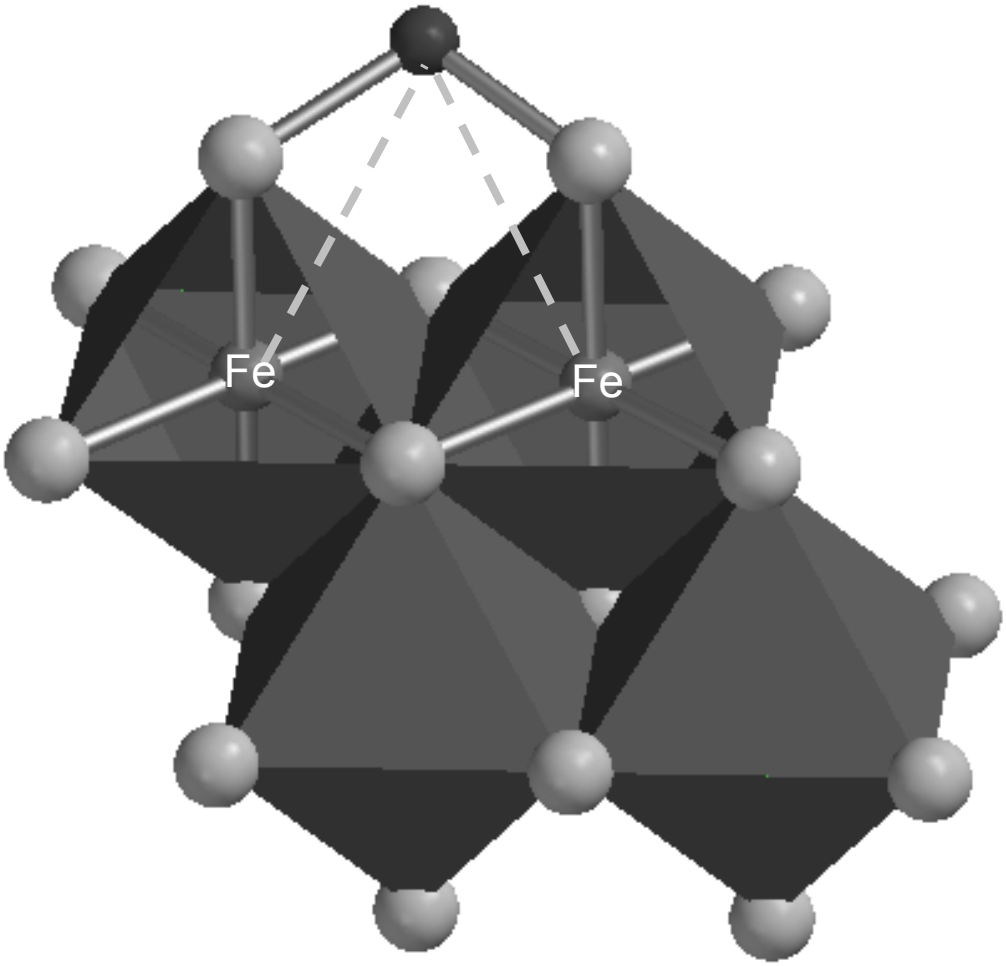

Figure 8

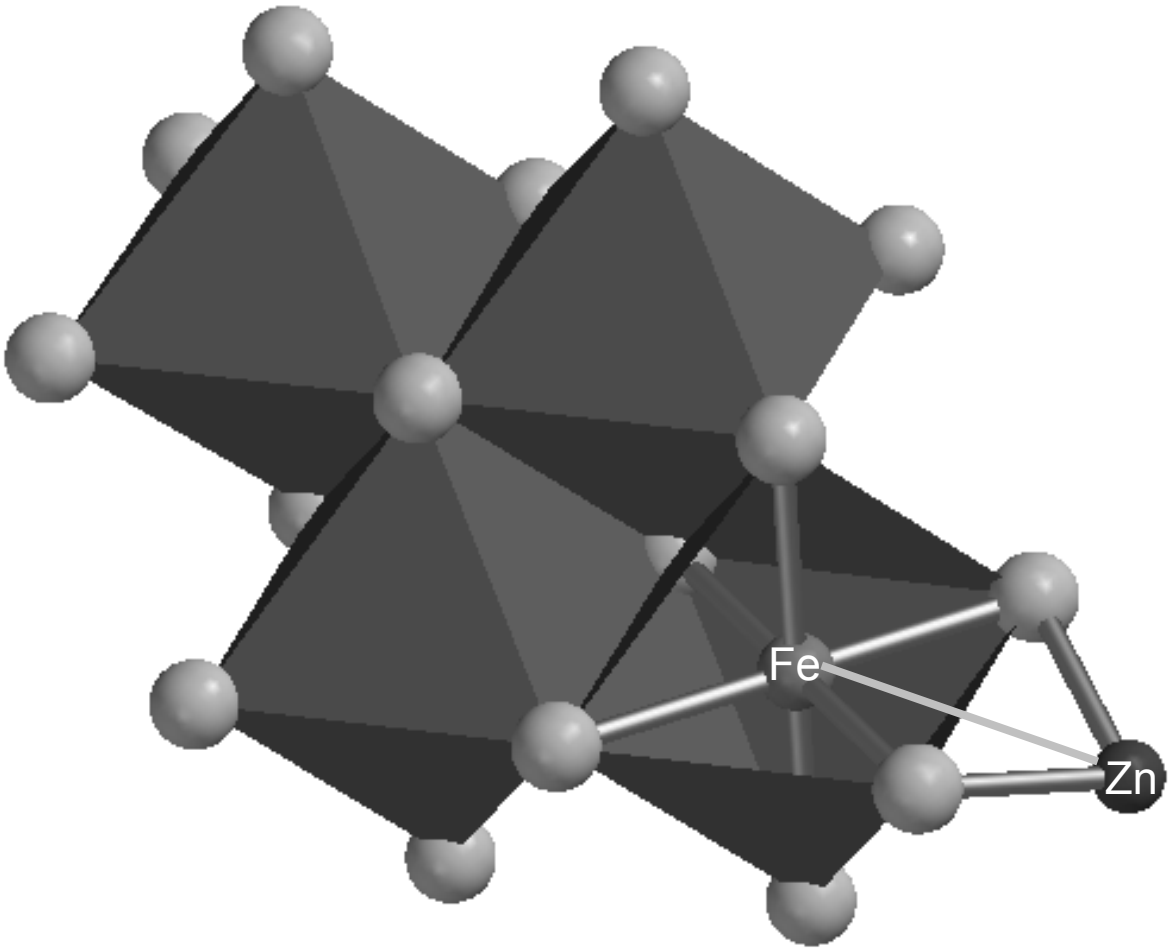

Figure 9

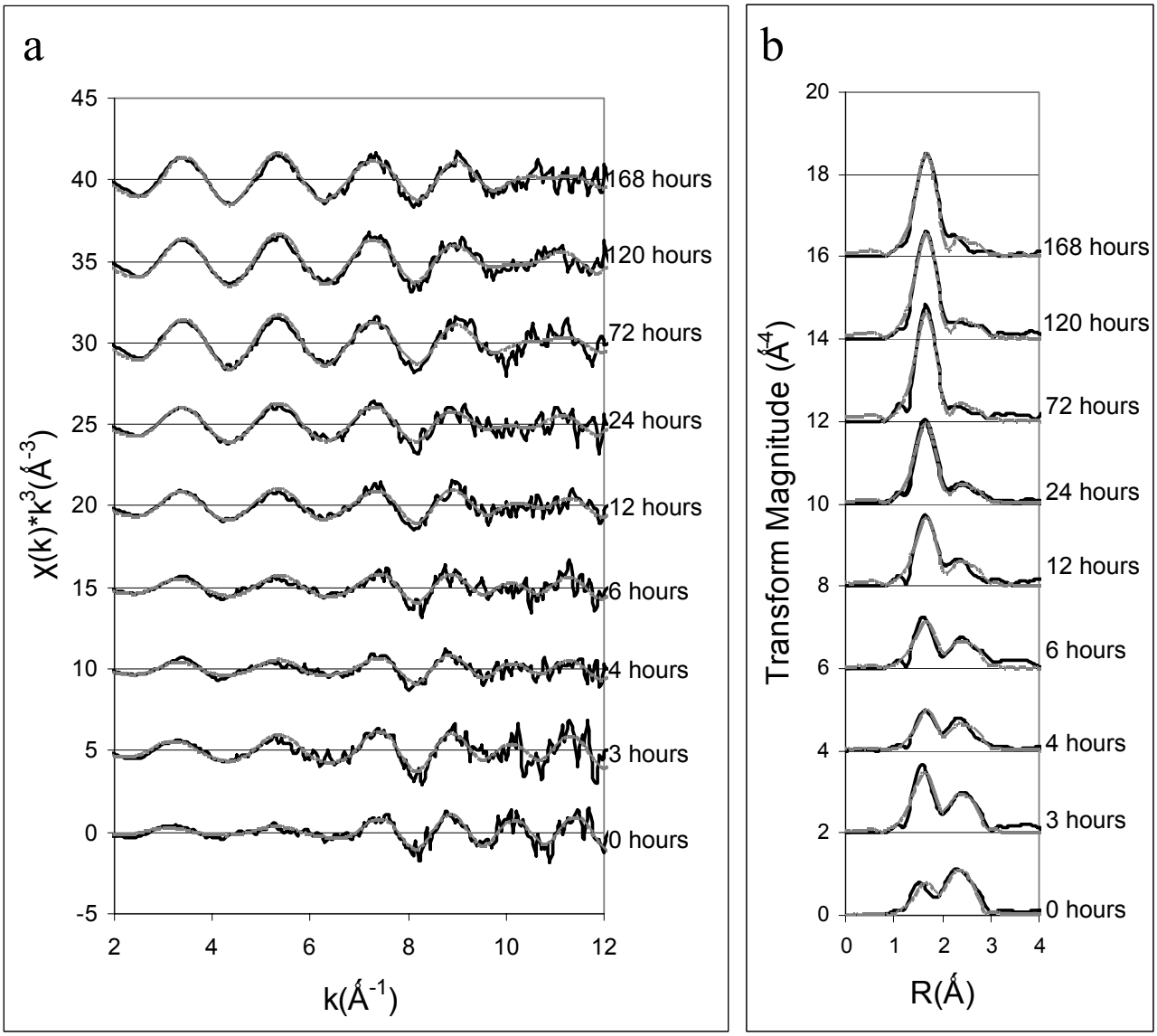
a
45
40
35
30
25
20
15
10
5
0
-5
2
4
6
8
10
12
k(Å-1)
X(k)*k3(Å-3)
168 hours
120 hours
72 hours
24 hours
12 hours
6 hours
4 hours
3 hours
0 hours
b
20
18
16
14
12
10
8
6
4
2
0
0
1
2
3
4
R(Å)
Transform Magnitude (Å-4)
168 hours
120 hours
72 hours
24 hours
12 hours
6 hours
4 hours
3 hours
0 hours

Figure 10 (a,b)

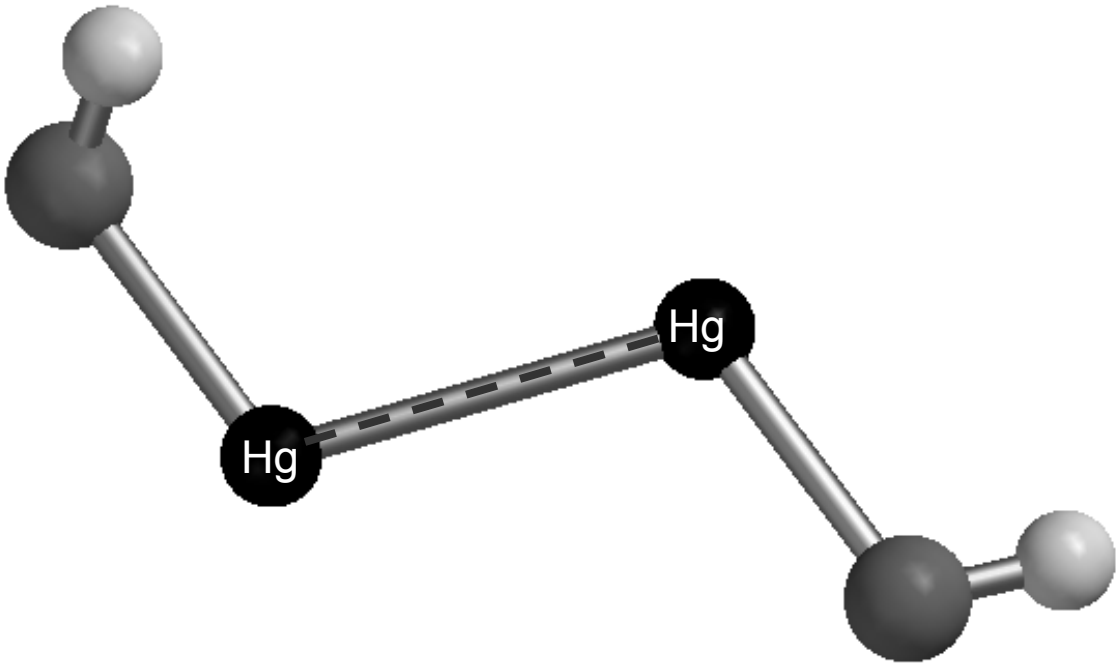

Figure 11

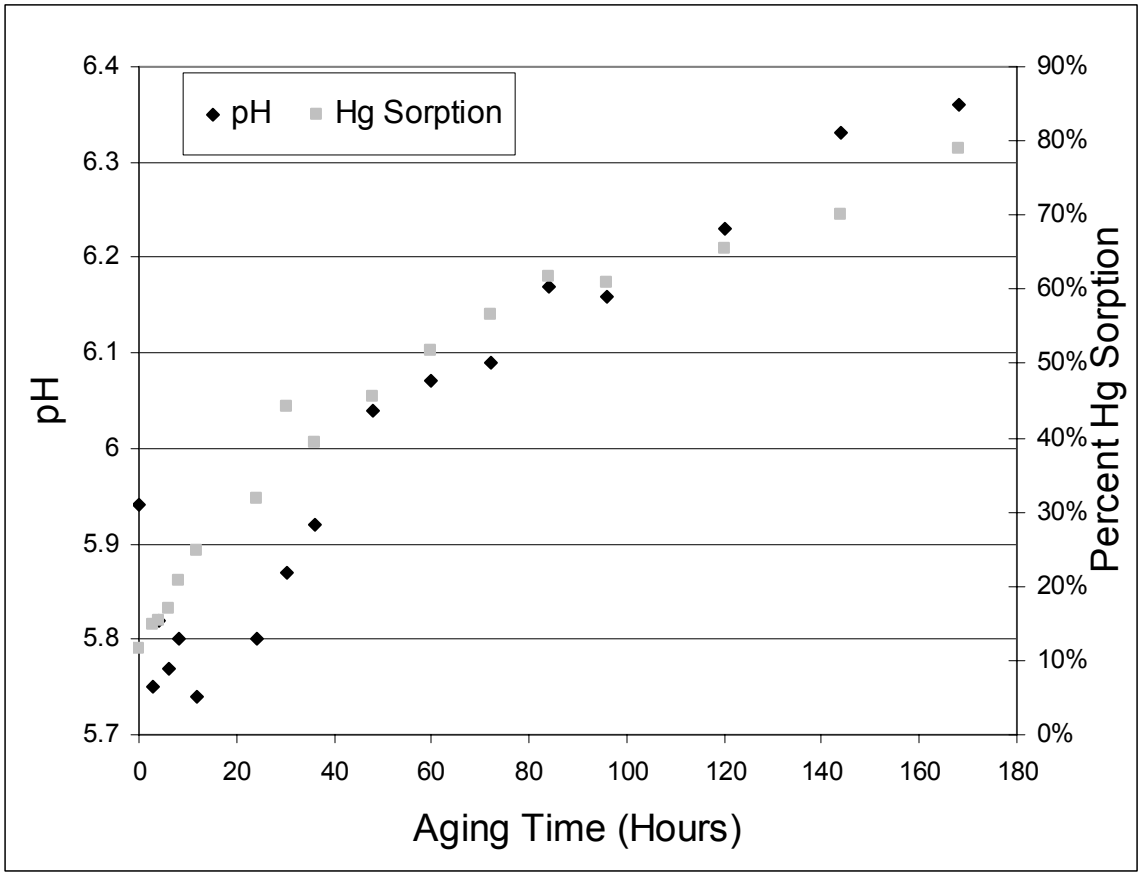
pH
Hg Sorption
6.4
6.3
6.2
6.1
6
5.9
5.8
5.7
90%
80%
70%
60%
50%
40%
30%
20%
10%
0%
Percent Hg Sorption
0
20
40
60
80
100
120
140
160
180
Aging Time (Hours)

Figure 12

Tables

Table 1: Zn K edge EXAFS fitting results for Zn(II) sorption to nanoscale goethite. Corresponding EXAFS spectra and Fourier transforms can be seen in Figure 7. CN = coordination number, R = interatomic distance, and σ^2 = Debye-Waller factor.

Table 2: Hg L_{III} EXAFS fitting results for Hg(II) sorption to nanoscale goethite. Corresponding EXAFS spectra and Fourier transforms can be seen in Figure 10. CN = coordination number, R = interatomic distance, and σ^2 = Debye-Waller factor.

Sample reaction time	Zn-O			Zn-Fe			Zn-Fe		
	CN	*R* (Å)	σ^2 (Å^2)	CN	*R* (Å)	σ^2 (Å^2)	CN	*R* (Å)	σ^2 (Å^2)
0 hours	3.7(3)	1.988(7)	0.007(2)	---	---	---	1.2(3)	3.43(2)	0.01[a]
2 hours	3.6(5)	1.97(1)	0.007(2)	---	---	---	0.7(5)	3.41(5)	0.01[a]
4 hours	3.7(3)	1.96(1)	0.0071(7)	---	---	---	1.4(5)	3.44(3)	0.01[a]
8 hours	3.5(4)	1.97(1)	0.006(1)	0.4(4)	2.97(6)	0.01[a]	2.5(5)	3.44(2)	0.01[a]
16 hours	3.7(5)	1.98(1)	0.007(2)	0.4(5)	3.00(7)	0.01[a]	2.3(6)	3.44(2)	0.01[a]
24 hours	3.5(4)	1.98(1)	0.007(1)	0.4(4)	2.97(6)	0.01[a]	2.3(5)	3.45(2)	0.01[a]
48 hours	3.5(4)	1.98(1)	0.007(1)	0.4(4)	2.99(6)	0.01[a]	2.2(4)	3.44(2)	0.01[a]
72 hours	3.7(5)	1.98(1)	0.008(2)	0.6(4)	3.00(5)	0.01[a]	2.2(5)	3.43(2)	0.01[a]
96 hours	3.6(5)	1.99(1)	0.007(2)	0.8(4)	3.00(4)	0.01[a]	2.2(5)	3.43(2)	0.01[a]

Table 1: [a] = set values; $S_0^2 = 0.81$; E_0 values ranged from 0.05 – 2.6 eV.

Sample reaction time	Hg-O			Hg-Hg		
	CN	*R* (Å)	σ^2 (Å^2)	CN	*R* (Å)	σ^2 (Å^2)
0 hours	0.6(2)	2.09(2)	0.007[a]	0.9(2)	2.51(2)	0.005[a]
3 hours	1.0(2)	2.04(2)	0.007[a]	0.8(4)	2.53(1)	0.005[a]
4 hours	0.7(2)	2.08(2)	0.007[a]	0.5(3)	2.55(1)	0.005[a]
6 hours	0.8(2)	2.06(2)	0.007[a]	0.5(3)	2.54(1)	0.005[a]
12 hours	1.2(3)	2.07(1)	0.007[a]	0.5(3)	2.54(1)	0.005[a]
24 hours	1.3(2)	2.060(8)	0.007[a]	0.4(2)	2.56(1)	0.005[a]
72 hours	1.8(3)	2.066(5)	0.007[a]	0.3(3)	2.53(2)	0.005[a]
120 hours	1.7(3)	2.062(9)	0.007[a]	0.3(2)	2.56(1)	0.005[a]
168 hours	1.7(3)	2.072(7)	0.007[a]	0.3(2)	2.52(1)	0.005[a]

Table 2: [a] = set values; $S_0^2 = 0.90$; E_0 values ranged from 7.7-13.0 eV.